PNAS Nexus, 2024, **3**, pgae510
https://doi.org/10.1093/pnasnexus/pgae510
Advance access publication 14 November 2024
Research Report

Topological mechanical states in geometry-driven hyperuniform materials

Sungyeon Hong[a,1], Can Nerse[b,1], Sebastian Oberst[b,*] and Mohammad Saadatfar[c,d,*]

[a]School of Cybernetics, College of Engineering, Computing and Cybernetics, The Australian National University, Canberra, ACT 2601, Australia
[b]Centre for Audio, Acoustics and Vibration, Faculty of Engineering and IT, University of Technology Sydney, Sydney, NSW 2040, Australia
[c]School of Civil Engineering, University of Sydney, Sydney, NSW 2006, Australia
[d]Department of Materials Physics, Research School of Physics, The Australian National University, Canberra, ACT 2601, Australia
*To whom correspondence should be addressed: Email: sebastian.oberst@uts.edu.au (S.O.); Email: mohammad.saadatfar@sydney.edu.au (M.S.)
[1]S.H. and C.N. contributed equally to this work.
Edited By C. H. Amon

Abstract

Disordered hyperuniform materials are increasingly drawing attention due to their unique physical properties, associated with global isotropy and locally broken orientational symmetry, that set them apart from traditional crystalline materials. Using a dynamic space-partitioning process, we generate disordered hyperuniform cellular structures where distinct patterns of pentagonal and heptagonal topological defects emerge within hexagonal domains. The microscopic defect dynamics are guided by local topological transitions, commonly observed in viscoelastic systems. This leads to a reduction in the system's structural entropy as hyperuniformity is attained, marked by the rise and fall of certain locally favored motifs. Further, we introduce an elastic hyperuniform material that exhibits evolving topological mechanical states in the continuum. Through vibration experiments and numerical analysis, we show energy localization around these defects, which is tied to the topological band gaps inherent to our geometry-driven material. We suggest that this robust dynamic mechanism influences a broad spectrum of disordered systems, from synthetic materials to biological structures guided by stigmergic interactions.

Keywords: Lloyd's algorithm, topological defects, hyperuniformity, wave propagation, defect engineering

Significance Statement

Hyperuniformity arises in wide-ranging fields, from quantum and classical systems to biological and cosmological models. Using Lloyd's algorithm as a foundation, we present a disordered hyperuniform landscape that minimizes low-frequency scattering through a unique vibrational band structure. Additionally, we identify a distinct band gap at topological interfaces, enriching multiband topological states. These findings are instrumental for the design of next-generation vibro-acoustic metasurfaces, acoustic devices, and sensors, offering enhanced robustness and broadband dynamic capabilities.

Introduction

Initially introduced as a new state of matter two decades ago, hyperuniformity has been observed in wide-ranging fields of physics and life sciences (1–6). Characterized by a suppression of density fluctuations at large length scales, hyperuniformity accounts for a hidden order in packing and tiling problems (7, 8) serving as a descriptor for nonequilibrium states or phase transitions in general (9, 10). Well-known examples include maximally random jammed packings of hard spheres (11, 12), the arrangement of avian photoreceptor cells (13) as well as the galactic distribution of the early universe (1). The interest in hyperuniformity has only been amplified and extended to engineering fields by the discovery of 2D disordered hyperuniform silica (14) and synthesized amorphous graphene (15) as shown in Fig. 1D. Hyperuniform materials are known not only to produce large, complete photonic band gaps (16–19) but also to contribute to enhanced vortex pinning in superconductors (20).

Given a point pattern, it is diagnosed as hyperuniform if it does not possess infinite-wavelength fluctuations, leading to a vanishing structure factor in the small wavenumber limit (see Fig. S1B) indicative for that specific crystallographic planes do not diffract incident radiation (2).

In mathematical terms, denoting by $N(R)$ the number of points contained in a d-dimensional spherical observation window of radius R, the local number variance σ_N^2 is defined as follows:

$$\sigma_N^2(R) = \langle N(R)^2 \rangle - \langle N(R) \rangle^2. \tag{1}$$

Competing Interest: The authors declare no competing interests.
Received: March 17, 2024. **Accepted:** October 18, 2024

If $\sigma_N^2(R)$ of the system grows slower than the window volume in the large-R limit, i.e. slower than $\mathbb{R}^d$, the system is hyperuniform (2, 24). Hence, any perfect crystalline lattice is hyperuniform with an asymptotic growth of $\sigma_N^2(R) \sim \mathbb{R}^{d-1}$ i.e. the variance grows as the surface area, and this property is shared with many types of quasi-crystals (25).

Among a broad class of hyperuniform systems with a varied degree of disorder, we are particularly interested in those systems generated by many-body interactions based on the geometric relations between near-neighbors. Earlier, Klatt et al. (8) proposed a geometric centroidal process, called Lloyd's centroidal Voronoi algorithm (Lloyd's algorithm, hereafter), as a simple and fast method to obtain disordered hyperuniform point configurations in both two and three dimensions. The Lloyd's algorithm runs iteratively to homogenize a spatial distribution of points by moving every point to the centroid of the corresponding Voronoi cell at each iteration step and has been applied to various engineering domains (26–29).

The algorithm demonstrates a purely geometric diffusive process, where nearest-neighbor interactions lead to a collective rearrangement of points, reminiscent of entropic systems (30–33). The resulting hyperuniform configurations consist of a small fraction of 5-fold or 7-fold point defects, known as *topological defects*, embedded in hexagonal domains (34).

Near perfect hexagonal patterns with defects are commonly encountered in nature. Figure 1 presents the Voronoi landscape of a disordered hyperuniform configuration generated by the Lloyd's algorithm along with examples of real-world systems bearing similar defective hexagonal patterns, including insect-built structures and materials. Motifs at the surface of arthropodic integuments (e.g. exoskeleton of Collembola) comprise a variety of periodic, hierarchical structures (35). Intrigued by these structures, the field of bio-informed (as opposed to bio-inspired) material science (36) emerged and the general question arose, whether the underlying formation rules of hyperuniformity and related defects could be mathematically recovered or controlled in engineering applications (37, 38).

We use Lloyd's algorithm to generate disordered hyperuniform[a] (DHU) configurations by deploying various randomly disordered initial conditions as input. We find that the dynamics of the Lloyd process is facilitated by plastic events, namely T1 transitions (39), which have been frequently observed in aqueous foams and cellular tissues (40). Using an entropic argument, we demonstrate the hierarchy of locally favored motifs in disordered hyperuniform configurations. Hyperuniformity indicates the existence of a particular symmetry (or atomic arrangement) that causes destructive interference in certain planes which influences the electronic band structure and opens band gaps. Band gaps are typical properties of optical but also vibro-acoustic materials. By using the finite element (FE) method, we therefore test numerically whether these defects induce topological interface modes and if these modes are efficient to alter vibro-acoustic material

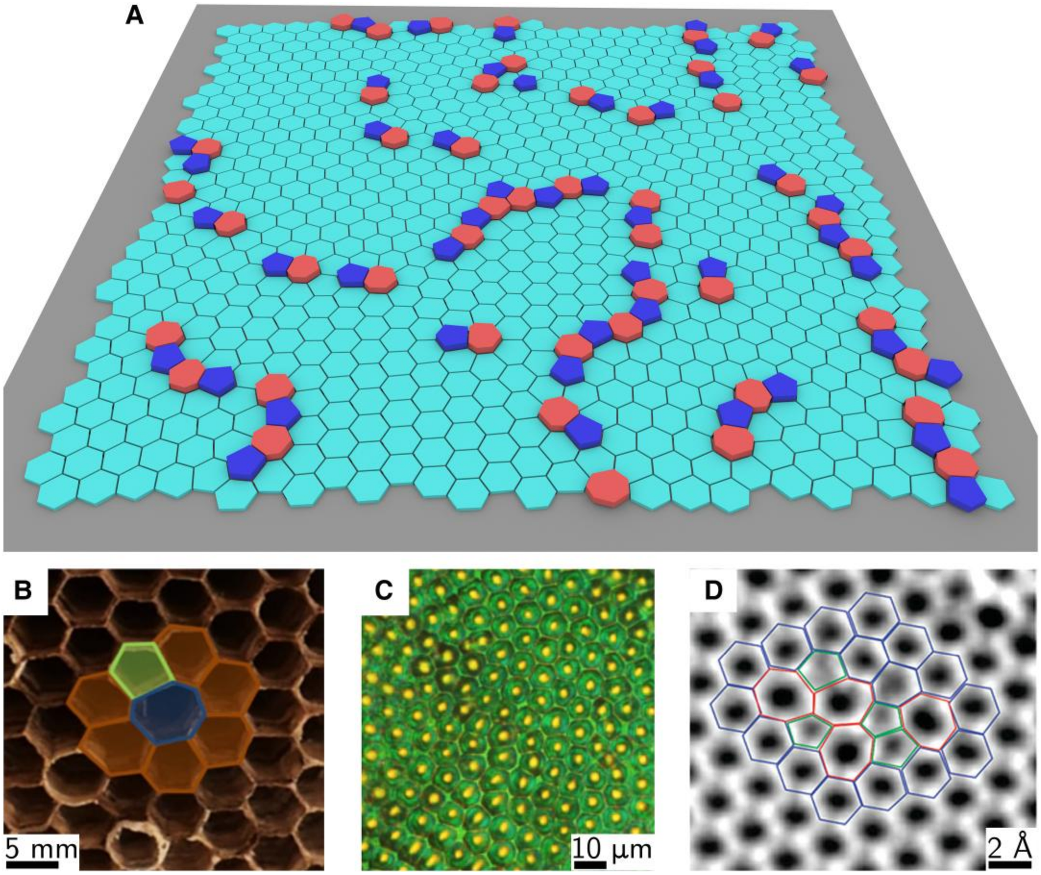

Fig. 1. Defective hexagonal patterns. A) The Voronoi landscape of a 2D disordered hyperuniform configuration generated by the Lloyd's algorithm. Pentagonal and heptagonal cells (topological defects) are highlighted by blue and red, respectively, while the remaining cells in cyan are hexagons. B) A close-up shot of a nest of the Australian paper wasp nest (*Polistes wattii*) (21). C) An optical micrograph of the exoskeleton of the glorious beetle (*Chrysina gloriosa*) (22). D) Stone–Wales (SW) defect, a common type of topological defect, found in a perturbed graphene layer, adapted with permission from Ref. (23). (Copyright 2008 American Chemical Society.) Overlaid outline consists of pentagons (green), heptagons (red), and hexagons (blue).

properties of a larger 3D printed structure (details in Materials and methods). We then aim to verify our findings under an experimental scheme of vibro-acoustic testing to visualize energy localization on a planar hyperuniform material. We demonstrate the existence of topological interface states for the first time using a geometry-driven 2D elastic hyperuniform system, which may catalyze the design of materials with bespoke vibro-acoustic properties.

Results

As a statistical ensemble for input data to the Lloyd process, we prepare twenty realizations (point patterns) of each type of the following stochastic point processes: Poisson point process (Poisson-PP), random sequential addition particle packing (RSA-PP), and Thomas point process (Thomas-PP) (41). Each point pattern contains N-many points, ranging from $N = 10^2$ to $N = 10^4$. In the process of Lloyd's algorithm, periodic boundary conditions are applied to evolve the system (see Materials and methods for more details). The Voronoi landscape of an initial random point pattern comprises various types of polygonal cells (Fig. S1A). At its termination, the majority of these cells settle into the hexagonal shapes, while the remaining cells take on either pentagonal or heptagonal shapes connected to each other to create string-like patterns up to a certain size.

Defect formation and annihilation mechanism

By repeating the process of fragmentation and aggregation throughout the ordering transition, defect components prevent the system from directing towards its global minimum energy landscape (see Eq. 6), a defect-free hexagonal lattice. Behind the scene of defect formation and annihilation, the sole mechanism for local reconfiguration is found to be a T1 transition, which refers to a topological rearrangement of four-cell aggregates (T1-quadruples): an edge shared by two cells of the quadruple flips to disconnect them and connect the other two by a new edge through neighbor exchange as depicted in Fig. 2A. Since the system is closed, there are no changes in the total number of points in each evolving system throughout the Lloyd process, and periodic boundary conditions are applied to eliminate boundary effects, therefore T1 transitions are the only mechanism responsible for defect generation and annihilation. T1 transitions are known to be fundamental to the plastic yielding of 2D liquid foams (39, 42) as well as to dynamics of cellular tissues (43–46).

Figure 2B displays a significant drop of the frequency of T1 transitions at an early stage of the evolution through the Lloyd process. The highly suppressed T1 activities after approximately $t = 100$ suggests the onset of a rigidity transition of evolving 2D systems through the Lloyd process. Combined with the plateau regime from around $t = 100$ in the mean square displacement (MSD) analysis shown in Fig. S1B, this finding aligns with recent studies suggesting that T1 transitions can serve as a geometrical criterion for *dynamical arrest* (47, 48). To thoroughly characterize this phenomenon, we conducted a range of analyses, including the static structure factor, MSD, and four-point susceptibility (see Fig. S1 in "Dynamical arrest along the Lloyd iterations" section). Our comprehensive analyses reveal spatiotemporal dynamic heterogeneity akin to glassy dynamics in our system.

Further, we have conducted a comprehensive simulation varying the initial conditions and system sizes (i.e. number of points). The results are shown in Fig. 2C, which demonstrates the consistency and reliability of T1 frequency behavior across varying system sizes and initial conditions. A graphical presentation of

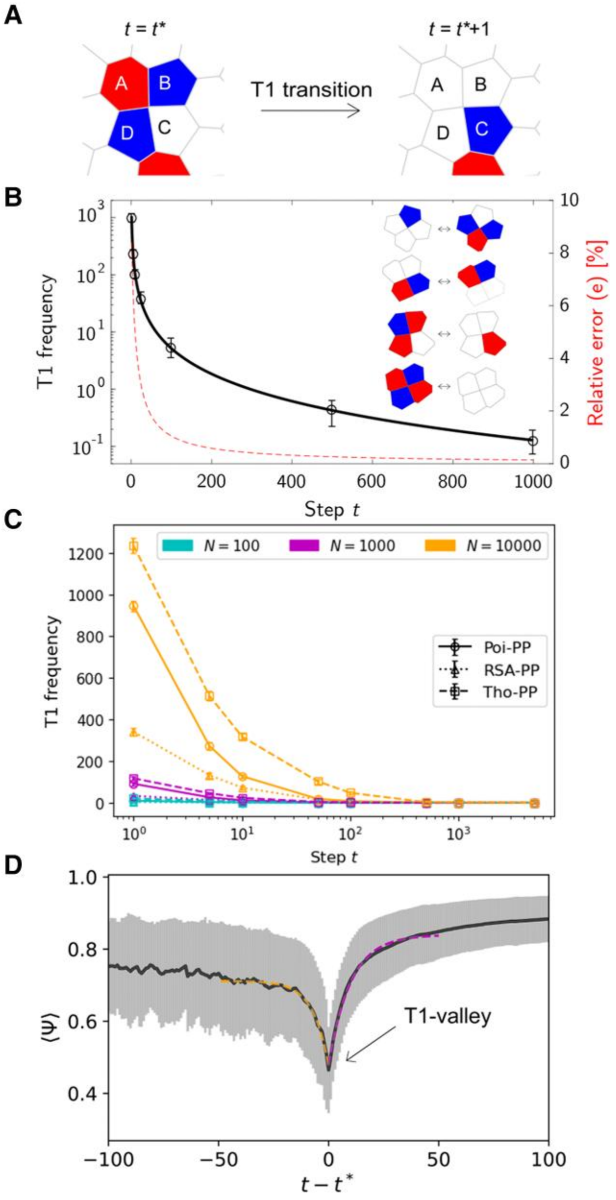

Fig. 2. T1 transitions governing cell dynamics. A) A T1 transition takes place for a four-cell aggregate ABCD ("T1-quadruple") at step $t = t^*$. Cell A and C at step $t = t^*$ are disconnected by a flipping edge through a T1 transition that connects cell B and D at $t = t^* + 1$. B) The T1 frequency averaged over twenty realizations of Poisson point process of $N = 10^3$ points rapidly drops as systems evolve into hyperuniform states along the Lloyd process. Relative error percentage highlights the fast convergence. Inset shows the major four types of T1 transitions that involve T1-quadruples consisting of polygonal cells with five (blue), six (white), and seven (red) edges. C) T1 frequency as a function of Lloyd iteration steps (Step t) for different system sizes ($N = 100$, $N = 1{,}000$, $N = 10{,}000$) and point processes (Poisson-PP, RSA-PP, Thomas-PP) for initial conditions. The plot illustrates the decrease in T1 frequency with increasing steps, highlighting consistent behavior across different initial conditions and system sizes in the dynamical evolution of the system. D) The mean polygonal symmetry $\langle\Psi\rangle$ of T1-quadruples of an evolving Poisson-PP of $N = 10^3$ points within a step range $t \in [0, 200)$ is plotted against $t - t^*$, where t^* denotes the time step where each T1-quadruple undergoes a T1 transition. The averaged symmetry values over all T1-quadruples captured during the first 200 iterations are represented by a bold black line, and the standard deviations along the steps are shown as gray error bars. The dashed curve on each side of $t - t^* \leq 0$ (orange) and $t - t^* \geq 0$ (magenta) is an exponential fit. The two curves meet to form a "T1-valley" at $t - t^* = 0$. This valley represents a universal drop of $\langle\Psi\rangle$ of T1-quadruples right before the T1 transition, followed by a sharp increase in their mean symmetry values after T1 transition. The displayed T1-valley at $t = t^*$ has $\langle\Psi\rangle = 0.44 \pm 0.12$.

evolving systems starting from three initial configurations (Poisson-PP, RSA-PP, and Thomas-PP) for a system size of $N = 1{,}000$ is presented in "T1 transition and initial conditions". This inclusion underscores the robustness of our findings and highlights the generality of the observed dynamical evolution. These results support the reliability of our findings and provide evidence for the consistent dynamical behavior observed across different system sizes and initial conditions.

In general, cellular dynamics resulting in collective migration of cells or complex structures in biological models is a result of mechanical activity or chemical signaling (49). However, since the Lloyd process is purely geometric, it is not obvious what criteria for local instability trigger T1 activities. It is hence critical to find a geometric concept analogous to a stress parameter to account for cell mobility in our study. Based on the observation that there is a change in member cell types of a T1-quadruple before and after the T1 transition,[b] we therefore consider the k-atic order parameter $\psi_k(\mathbf{x})$ for each cell generated by $\mathbf{x}$, which is defined as follows:

$$\psi_k(\mathbf{x}) = \frac{1}{k}\sum_{\mathbf{y}} e^{ki\theta_{xy}}, \qquad (2)$$

where the sum runs over the nearest neighbors $\mathbf{y}$ of $\mathbf{x}$ with θ_{xy} denoting the angle between the vector $\overrightarrow{xy}$ and its reference axis. Note that $|\psi_6| = 1$ indicates a perfect, local hexagonal symmetry. To determine a T1 criterion, we measure the mean polygonal symmetry $\langle\Psi\rangle$ of each T1-quadruple by taking the mean value of Eq. 2 of its four member cells. For the cell ABCD in Fig. 2A, we arrive therefore at $\langle\Psi(\mathrm{ABCD})\rangle = \frac{1}{4}(|\psi_7(\mathrm{A})| + |\psi_5(\mathrm{B})| + |\psi_6(\mathrm{C})| + |\psi_5(\mathrm{D})|)$.

We look at the temporal evolution of the mean symmetry $\langle\Psi\rangle$ of T1-quadruples of an evolving system in Fig. 2D. The mean symmetry curve for each T1-quadruple is translated by the corresponding pre-T1 step denoted by t^* along the time axis, so that we can see collapsing curves for all those T1-quadruples captured within the iteration step range in consideration. We then average their mean symmetry values at $t - t^*$ for each Lloyd step at time t. Interestingly, there exists a singularity of the mean symmetry of T1-quadruples at $t = t^*$: $\langle\Psi\rangle$ values shape a minimum by decreasing until the T1-quadruples undergo T1 transitions, followed by a sharp increase in their symmetry right after the local topological rearrangement. Such a "T1-valley" in mean symmetry of the member four cells can be fitted by an exponential function on each side for $t < t^*$ (pre-T1 steps) and for $t > t^*$ (post-T1 steps) and is found to be universal regardless of number of the points in the system.

Locally favored motifs and entropic ordering

The Lloyd's algorithm is inherently entropic and can produce infinitely many distinct realizations in DHU states (8). Therefore, a key question in this context is how the delicate interplay of local dynamics and global entropy minimization can drive the system towards a defective DHU phase. To address this question, we consider the notion of *structural entropy* that counts the number of distinct topological microstates in a system, based on graph isomorphism (50). To this end, we construct the Delaunay network (51) onto a point pattern (dual counterpart of the Voronoi landscape), which is often used to find local structural motifs and to identify how they are clustered and form a network amongst themselves (50, 52). On top of the Delaunay network, we apply a grid of various sizes and move it along the system to extract local motifs (graphs) of size n (i.e. number of nodes) with every node having a degree ≥ 2 (Fig. 3A). The collected local motifs can then be classified into distinct classes of graph isomorphisms, based on the number of nodes and the connectivity through edges[c].

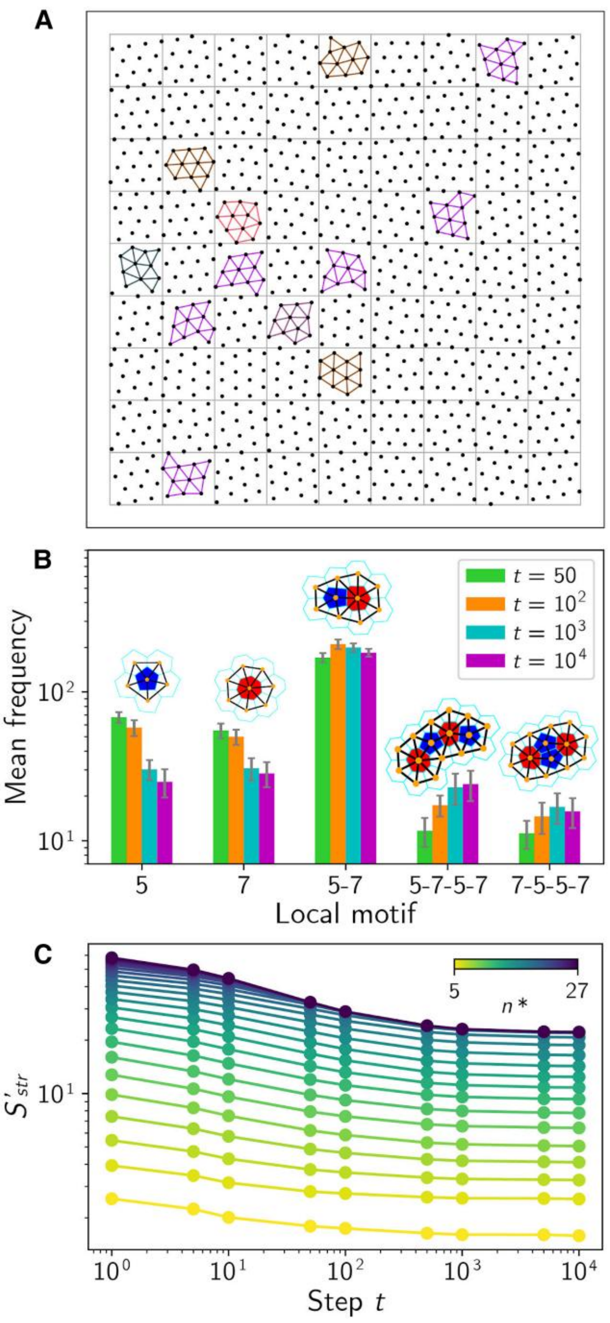

Fig. 3. Locally favored motifs and structural entropy. A) Local motifs of size $n = 11$ are captured in a grid onto a point pattern. Isomorphic graphs are of the same color. B) The mean frequency of locally favored motifs, consisting of k-fold point defects and their first neighboring points (with their hexagonal Voronoi cells with cyan edges), at selected steps $t = 50, 10^p$ ($p = 2, 3, 4$) of evolving systems, averaged over twenty realizations of Poisson-PP. Error bars indicate the standard deviations of the number of motifs. C) The temporal evolution of the normalized structural entropy $\mathcal{S}'_{\mathrm{str}}$ cumulative to extracted motifs of size up to n^*. The linear lines are guide to the eye.

We put our focus on five of the most popular types of local motifs associated to 5-fold and 7-fold point defects along with their first neighbors (insets in Fig. 3B). For instance, the motif built on a 5-fold defect and its neighboring points is denoted by type "5" (graph size $n = 6$), the one for a 7-fold defect with its neighbors by type "7" ($n = 8$), and a double defect and its neighbors by type "5–7" ($n = 10$). Note that motifs representing quadruple defects have degeneracy of two with either type "5-7-5-7" ($n = 16$) or type "7-5-5-7" ($n = 14$). Figure 3B displays the temporal evolution of the mean frequency of such motifs at selected steps $t = 50,\ 10^p$ ($p = 2, 3, 4$) of evolving systems with $N = 10^4$ points. We observe a decreasing trend for both isolated defect motifs (types 5 and 7), whereas there exists a sharp increase in type 5-7-5-7 motifs and a similar increase yet with a slight decrease from $t = 10^3$ to $t = 10^4$ for type 7-5-5-7 motifs. The motif of type 5-7 (i.e. double defect motif) appears stable throughout the Lloyd process and stands out with the highest population as an all-time favorite.

After collecting local motifs of various sizes, we compute the structural entropy $\mathcal{S}_{\mathrm{str}}$ as follows (50):

$$\mathcal{S}_{\mathrm{str}}(n) = -\sum_{\mathcal{C}_n} \mathbb{P}(\mathcal{C}_n) \ln \mathbb{P}(\mathcal{C}_n), \tag{3}$$

where the summation runs through distinct isomorphism classes $\mathcal{C}_n$ of graphs of n nodes, and $\mathbb{P}(\mathcal{C}_n)$ denotes the probability of finding graphs in $\mathcal{C}_n$. By taking the maximum size n^* of graphs into account, we plot the normalized entropy in Fig. 3C by using the definition below:

$$\mathcal{S}'_{\mathrm{str}}(n^*) := \frac{1}{n^* - 2} \sum_{3 \le n \le n^*} \mathcal{S}_{\mathrm{str}}(n), \tag{4}$$

where we consider $5 \le n^* \le 27$ as the maximum range. Along with the growing number of points with 6-fold symmetry as well as the emergence of defect species of connected 5-fold and 7-fold point defects, we verify the decreasing global structural entropy as shown in Fig. 3C.

Topological states in elastic DHU systems

When two elastic systems with different topological invariants are edge-to-edge joint, the topological interface states can be predicted to emerge according to the so-called surface impedance match condition (54). Using a Lloyd-generated DHU system ($N = 100$) consisting of double and quadruple defects in template of a wireframe structure (Fig. 4A), we demonstrate the numerical and experimental observation of topological interface states. In the example using a realization of Thomas point process (Thomas-PP)—see Materials and Methods, as input where quadruple defects of type 7-5-5-7 exists, the projected band structure in Fig. 4B is calculated based on the lattice constant of $a = 172.48$ mm in a square Brillouin zone. A flat band of transverse mode at the frequency of $\omega/\omega_6 = 0.977$ or 2, 859 Hz, where $\omega_6 = 2{,}927$ Hz refers to first bending frequency of a hexagonal cell, between the optical bands is observed in the projected band structure along k_x-direction.

To investigate whether the spectral patterns of such interface states are influenced by T1 transition and whether they can be identified through the dynamics of individual cells, we numerically extracted the eigenfrequencies and mode shapes of hexagonal cells and local motifs of the DHU wireframe structures. The first two bending modes and shear modes are visualized as a function of normalized frequency and cell area, as shown in Fig. 4E. Two additional inputs with RSA-PP and Poisson-PP were considered for comparison (Figs. 4F and 4G). At the time step $t = 5{,}000$, the entropic state of each wireframe structure can be deduced through the hexatic order $|\psi_6|$ and the number and shape of local motifs that are frozen in the hexagonal domain (Figs. S4–S6). While hexagonal cells in a lattice structure feature eigenmodes with identical frequencies associated with 6-fold rotational symmetry (C_6) (Figs. S7A and S7B), this symmetry is broken in DHU structures resulting in decoupled modes. We observe that DHU structure with Thomas-PP input retains a more uniform modal distribution at its converged state with closely spaced eigenvalues owing to high $|\psi_6|$. At the frequency band associated with topological interface modes observed in the band structure (Fig. 4C) a similar modal pattern exists for the 7-5-5-7 motif (Fig. S7C) with its frequency also coinciding with the first bending mode of the hexagonal cells.

As the distance between local motifs in a DHU pattern increases, as in the case of RSA-PP and Poisson-PP, the modal interaction between them decreases, resulting in a weaker coupling between pairs of 5-7 motifs and a stronger coupling with the bulk modes of the hexagonal domain. In RSA-PP, we observe that this results in a narrower band where topological interface modes are present. Conversely, in Poisson-PP, by virtue of longer chain of motifs and larger in number, the modal activity between the individual motifs increases inducing a wider topological band.

We fabricate an elastic DHU metamaterial (details in Materials and methods) to experimentally validate the existence of topological states (Fig. 5). The real-space distribution of the displacement field is excited with a transverse sinusoidal input applied along the interface in the defective region using an electrodynamic shaker, whose connection to the wireframe structure is shown in Fig. 5B. Scanning laser Doppler vibrometry is used to measure the velocity profile across the surface of the sample. We find that vibrations are located mainly at the interface between two pentagons in the defected region and attenuate dramatically into the bulk of the material, which coincides with the field distribution of the eigenmode of the flat topological band (Fig. 4C). The flat band renders thus the topological interface mode independent from bulk modes as also shown in the transmissibility spectra (Fig. 5C). Vibration energy scatters into the right edge which is consistent with simulated results as presented in Fig. S4.

Conclusion and discussion

In this study, we have focused on the complexities of disordered hyperuniform geometries generated via Lloyd's algorithm. Our findings indicate that as point patterns undergo Lloyd's iterative refinements, the neighbor exchange among points corresponds to what is fundamentally known as a T1 topological transition. Importantly, this transition acts as the sole microscopic mechanism responsible for both the formation and subsequent annihilation of defects during the Lloyd computational process. We introduce the notion of mean cell symmetry within T1-quadruples, positioning it as a pivotal geometric criterion that demarcates the tolerable limits of topological configurations cells can endure before undergoing a T1 transition. Remarkably, this phenomenon of symmetry tolerance finds parallels in multiple systems: in biological confluent tissues, a mechanical energy functional barrier must be overcome for a T1 flip to occur (44, 45). Similarly, in evolving aqueous foams, the T1 topological flip underpins the foam's intricate viscoelastic rheology (55–57). This complex behavior manifests as dynamical arrest in our mechanical, macroscopic wire mesh system (see Fig. S1). These connections offer a consolidated perspective for understanding the ubiquity of topological transitions in a diverse range of physical and biological systems, thereby enriching our comprehension of how cell-level activities universally dictate defect management across length and time scales and material types.

By adopting the concept of structural entropy, we have verified that the ordering transition through the Lloyd's algorithm results

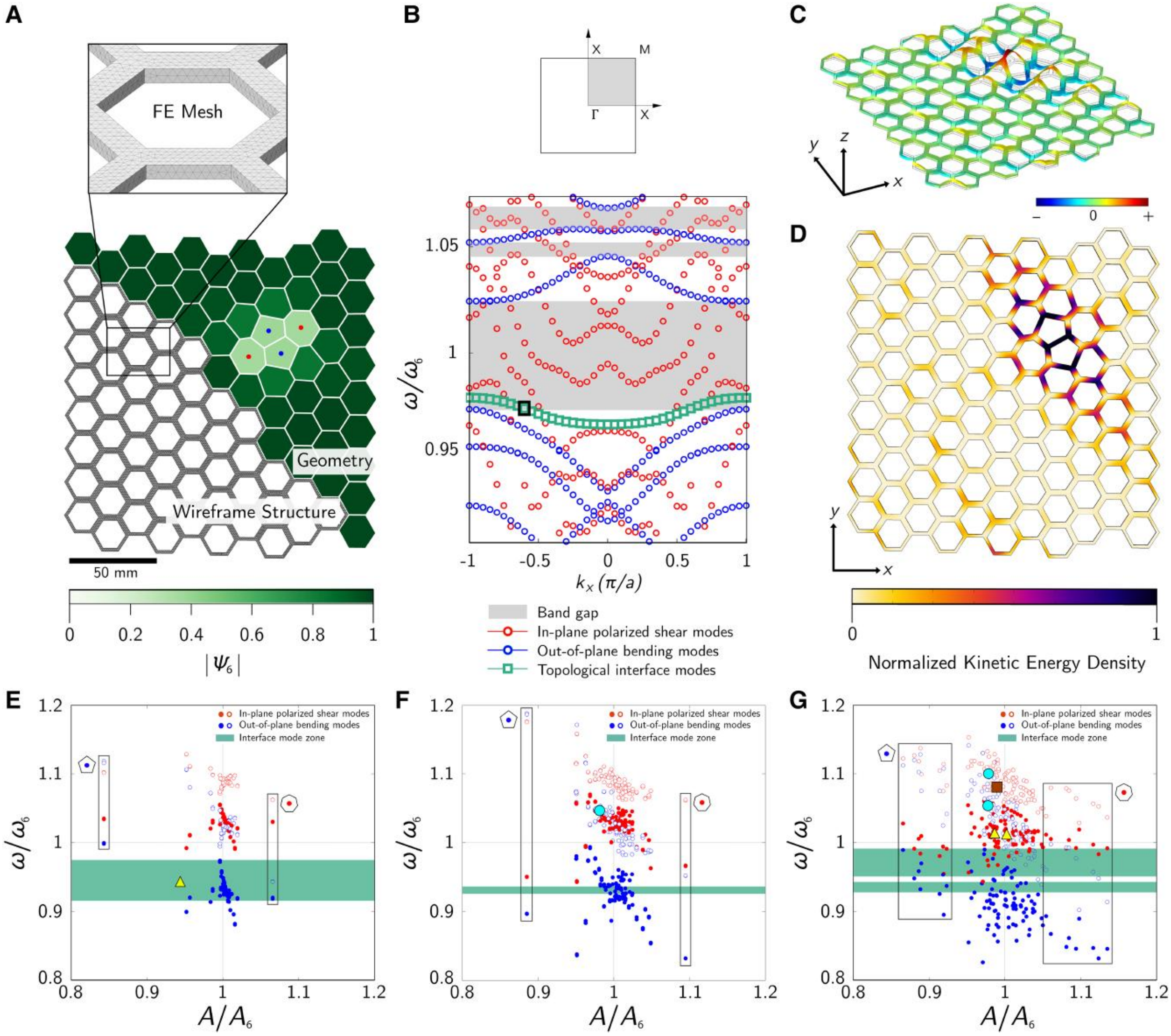

Fig. 4. Topological interface modes arising in DHU systems in the template of a wireframe structure. A) Hexatic order $|\psi_6|$ of a DHU system ($N = 10^2$, $t = 5{,}000$) obtained by using a realization of Thomas-PP as input and the resulting 7-5-5-7 local motif. B) Dispersion diagram of the DHU wireframe shown in A with a lattice constant of a = 172.48 mm. Eigenfrequencies are normalized by the first bending mode frequency of the hexagonal cell ($|\psi_6| = 1$, $f = 2{,}928$ Hz)—periodically arranged in the equivalent design space. In-plane polarized shear modes and out-of-plane bending modes are shown by red and blue circles, respectively. Topological interface modes, denoted by green markers, are exhibited within the band gap associated with the out-of-plane bending mode, which is shown by the gray shaded regions. C) demonstrates the Bloch mode at $k_x = -0.6$, which is shown in B by a black square marker. D) Normalized kinetic energy density profile of the DHU structure is shown at $k_x = -0.6$. Accumulation of the kinetic energy around the defect cells is visible by the darker colors between the pentagons. E) Modal density is plotted as a function of normalized eigenfrequency of isolated 5,7-gon cells and normalized cell area (A/A_6), where A is the area of the 5,7-gon cells and A_6 is the area of the hexagonal cell. Solid and hollow circles are the first and second bending/shear modes of a cell, respectively. Green shaded region corresponds to frequency intervals where interface modes are observed in the semi-periodic configurations—more details in SI. For comparison, modal density and resulting interface mode zones for DHU wireframe structures with F) RSA-PP and G) Poisson-PP as input are demonstrated, respectively. Eigenfrequencies of the local motifs strongly coupled with the hexagonal cells are denoted by cyan circles (5–7), yellow triangles (7-5-5-7 and 5-7-5-7) and brown squares—combination of the previous two motifs, as demonstrated in Fig. S7.

in the reduction of global entropy. Upon achieving disordered hyperuniformity with decreasing global entropy, a system also increases local entropy through certain types of locally favored motifs, which is concordant with the observation of heterogeneous network structures near the onset of rigidity transition (58). Such an entropic ordering is deemed crucial not only for our fundamental understanding of global ordering accompanied by microscopic disorder in the context of self-organization in a broad range of biological processes (59–61) and soft matter systems (30–32, 52, 62–70), but also for the design of novel materials with new optical, mechanical, or as exemplified here vibro-acoustic properties (16–19, 71–75).

The capacity to intentionally introduce disorder in materials hinges on our ability to assess their structural properties through quantifiable metrics. Within the framework of this study, we introduced two strategically placed double defects within a hexagonal domain, effectively inducing a controlled degree of disorder. These induced defects are retained in a wireframe configuration, the geometric density distribution, i.e. ratio of nonvoid sections to total volume, of which aligns with a characteristic

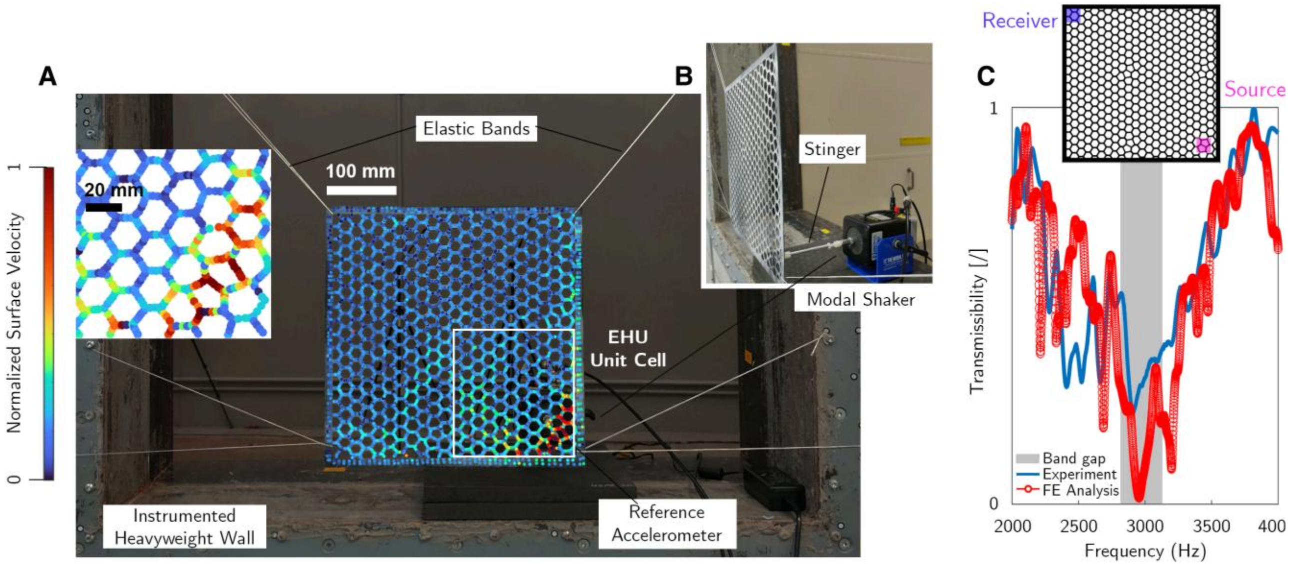

Fig. 5. Experimental validation of source localization. A) Instrumentation of the test sample constructed with 2-by-2 array of the DHU unit cell under sinusoidal sweep excitation by a modal shaker. The test sample is suspended by elastic bands on a heavyweight wall construction to minimize boundary excitation. Test facility is a reverberation chamber at UTS Tech Lab, whose background noise level conforms to ISO 10140 (Fig. S8 for more detail). The white outline denotes the DHU unit cell. In colored overlay shows the velocity profile of the DHU system at $f = 2{,}832$ Hz, where the source localization around the 7-5-5-7 defect is shown by red color. The vibration attenuation at the band gap is visible away from the source. B) A close-up shows the connection of the modal shaker into the sample at the defect region by a stinger. C) Normalized transmissibility curve representing the energy propagation from the source to a receiver location is shown for experiment and FE analysis. At the band gap region (gray shaded), correlation of the response between source and receiver locations is minimized owing to bending wave attenuation.

density threshold of approximately 0.7, crucial for a shift in the system's structural attributes rather than apparent density (76, 77).

Defective metamaterials represent a fascinating area of research at the intersection of materials science (submicron scale) and engineering (macroscopic effects). The intentional design of defects will then allow harnessing intriguing phenomena, such as elastic wave control, (78), Fano resonances caused by an asymmetrical space distribution (79) and band gaps (16, 17). Fano resonances arise for a mechanical waves passing through the material, and its interference with defect-induced local resonant modes leading to sharp and asymmetric peaks in the material's response with very high Q factors, ideal for sensing applications (80, 81) and used in for the design of defected 1D phononic crystals for gas sensing (82). Meanwhile, band gaps are regions of frequency where vibrations or waves are effectively prohibited from propagating through the material, due to its carefully engineered structural imperfections (80, 82).

A deeper understanding of the underlying mechanism for a transition into a defective landscape can further catalyze development of novel materials or can lead to performance enhancement of existing materials in line with graphene or other promising 2D materials (83–85). As an extension of this study, controlled regimes over Lloyd's iterations can be considered; the control of defective landscapes in materials using self-organization would pioneer a direction in defect engineering. For instance, we may anchor designated lattice points in a system and let other randomly located points evolve around these points. Our preliminary results show that the added constraints give rise to different types of defective motifs that have not been observed in the uncontrolled regime. On the other hand, a smaller number N of points in a system is expected to give us more control and a deeper insight into final landscapes. Imposing various conditions to increase the mean frequency of certain motifs can enable the DHU system to support topological states in broadband. In this aspect, it would also be interesting to apply machine learning techniques to classify all the possible converged states for small N and use them as supercells for various analysis and to identify an arrangement of certain types of motifs for bespoke properties.

Materials and methods

Lloyd's algorithm

Given a point pattern, the Lloyd's algorithm iteratively updates the system by moving points to the centroids of the corresponding Voronoi cells. The converged disordered hyperuniform configurations via Lloyd's algorithm are associated to deep local energy minima of the "quantizer problem" (8, 86): a partitioning of space with cells of similar sizes whose centroids are almost matching the generating points of the corresponding Voronoi cells.

This corresponds to the minimization problem for the *quantizer energy functional* of a given set of points $\{\mathbf{x}_j\}_{j=1}^{N}$:

$$\mathcal{E}_q(V_{\mathbf{x}}) = \int_{V_{\mathbf{x}}} \|\mathbf{x}-\mathbf{z}\|^2 \, d\mathbf{z}, \qquad (5)$$

where $V_{\mathbf{x}}$ is the Voronoi cell associated to point $\mathbf{x}$.

That is, the algorithm minimizes the cell-wise quantizer energy of a given configuration, the sum of which can be re-scaled to be the dimensionless *total quantizer energy* as follows:

$$\bar{\mathcal{E}}_q = \frac{N^{\frac{2}{d}}}{d|\Omega|^{1+\frac{2}{d}}} \sum_{j=1}^{N} \mathcal{E}_q(V_{\mathbf{x}_j}), \qquad (6)$$

where N is the number of points $\mathbf{x}_j$ ($j = 1, \ldots, N$) in a d-dimensional simulation box $\Omega \in \mathbb{R}^d$. The quantizer energy minimization throughout the algorithm is done by using `Papaya2` (87). As systems evolve into disordered hyperuniform phases over the Lloyd iterations, their total quantizer energies $\bar{\mathcal{E}}_q$ converge approximately to 0.0808, which lies between 0.0833 ($\approx 1/12$) of a 2D square lattice and 0.0802 of a hexagonal lattice.

Initial random point patterns

We use *stochastic spatial point processes* to generate randomly disordered point patterns as input to the Lloyd's algorithm (41). Among a variety of stochastic processes, the following three types of point processes are chosen to prepare 2D input point patterns in our study.

1. Poisson point process (Poisson-PP) (41) is typically used to model a set of randomly scattered objects in space, such as an ideal gas ensemble, transmitters in a wireless network, particles colliding into a detector or trees in a forest. This process is characterized by the independence of number density restricted to disjoint sub-regions, representing lack of interaction between points. It is named so because the number of points in a sub-region A of a space is a random variable following a Poisson distribution with mean $\mu(A)$, where μ is a given intensity measure of the process.
2. Random sequential addition particle packing (RSA-PP) models a random packing of hard particles (disks in 2D; spheres in 3D). For a certain exclusion distance r, disks of radius r are sequentially inserted at random coordinates unless they intersect with existing particles; if a new disk intersects with any existing ones, the corresponding insertion is rejected, and the addition process goes on until the system saturates, i.e. until no more disk can be inserted. A point pattern can be obtained by taking the centers of the disks.
3. Thomas point process (Thomas-PP) consists of "parent" points and "offspring" points. After generating parent points via Poisson point process in a simulation box, each parent point is replaced by a cluster of offspring points of which coordinates are random variables from a normal distribution (independent of each other) and the number of which follows a Poisson distribution. Hence, it is likely to observe groups of points clumping together as a result of a Thomas-PP.

Each system in our study consists of N points in a square box of side length $L = \sqrt{N}$ (for the unit number density $\rho = 1$ with the unit of length $\ell = \sqrt{\rho}$). The algorithm runs to evolve each system with the periodic boundary conditions applied.

Material and sample fabrication

A commercial acrylonitrile butadiene styrene (ABS) plastic 3D printing material is used to fabricate the experimental wireframe structure with material density of $\rho = 1,050\,\mathrm{kg/m^3}$. The sample whose outer dimensions are 36.5 cm by 36.5 cm is fabricated by AON M2+ 3D Printer at the University of Sydney Manufacturing Hub (SMH) Core Research Facilities with a uniform material thickness of 1.59 mm and tolerance of 0.01 mm. Isotropic material model with linear elastic properties is used to fit the transverse deflection under dynamic excitation. Thus, we obtain the mechanical properties of the ABS plastic material as $E = 1.9$ GPa, Poisson's ratio of $\nu = 0.3$, and loss factor of $\eta = 0.009$.

Finite element simulation

We use the Solid Mechanics Module of the commercial software COMSOL Multiphysics (version 6.0) to predict the frequency domain characteristics of the hyperuniform wireframe geometry at different Lloyd iterations. We model the geometry, as seen in Fig. 4A for $N = 100$ obtained at Lloyd time-step $t = 5{,}000$, using tetrahedral quadratic elements. The maximum element size is set to 0.9 mm after performing a mesh convergence study showing that the mesh is sufficiently refined to ensure little to no differences in global deformation. The mechanical properties are extracted from a model updated fit using experiment data. The undeformed hyperuniform unit cell with periodic boundary conditions is used to calculate the band structure and eigenmodes, while 2-by-2 array of the unit cell with all free boundary conditions are used for material model updating, as detailed in Figs. S8 and S9. For calculating the transmissibility spectra, a nodal force in out-of-plane direction is implemented at broadband to represent the sweep signal. Point displacement probes are implemented at various locations on the geometry to collect the transmitted signal. The kinetic energy density is calculated from the cycle average velocity response.

Testing and analysis

A transverse wave is generated by a permanent magnet shaker with an integrated amplifier (The Modal Shop, MiniSmart Shaker K2004E01) and vibration is transmitted through a stinger rod that is epoxy-glued to the sample. At four corners of the sample, elastic connection is used to freely suspend the sample in mid-air using soft bungee cords, with end connections joined to a heavy-weight concrete wall to eliminate boundary excitation (88). We measure the sample's surface vibration using a scanning laser Doppler vibrometer (Polytec, PSV-500 Xtra) after surface-treatment using a nonaqueous reflective powder coating to increase reflectivity and reduce speckle noise. For laser measurement locations, a total of 7,900 nodes are defined corresponding to an average spatial resolution of 1.75 mm. A uniaxial IEPE accelerometer (Brüel & Kjær, Type 4533-B) is attached to the corner of the wireframe structure to measure the acceleration at a reference node to enable cross-power spectrum and operational deflection shape (ODS) calculations. Synchronized measurements are conducted by a trigger force sweep signal of 244.14 mHz resolution and a sampling frequency of 12.5 kHz. The time signal is linear averaged three times to minimize the noise and to increase coherence. All tests are conducted in an acoustic testing facility located at UTS Tech Lab, whose background noise level conforms to the ISO-10140 standards for sound insulation material testing (89). The transmissibility spectrum that is plotted in Fig. 5C is generated by taking the Fast Fourier Transform of the time signal and applying a Savitzky-Golay filter (90) in MATLAB using the `sgolayfilt` function. Then, the transmissibility is calculated by taking the ratio of output transfer function to input transfer function, i.e. $H = q_2/q_1$, where q_2 and q_1 are the transfer functions at the output and input locations, respectively.

Notes

[a] The resulting configurations are classified as "effectively" hyperuniform verified by the *hyperuniformity index* (see SI Eq. 6) (8). However, to emphasize the disordered nature of the converged systems with topological defects, we simply omit "effectively" and use the term *disordered hyperuniformity* (DHU) in this article.

[b] e.g. the four-cell aggregate ABCD in Fig. 2A has the form of a quadruple 7-5-6-5 at $t = t^*$ (pre-T1 step), which turns into a quadruple of 6-6-5-6 at $t = t^* + 1$ (post-T1 step).

[c] We used the software `nauty` (53).

Acknowledgments

S.H. acknowledges the Visiting Scholar appointment with the Centre for Audio, Acoustics and Vibration (CAAV) at UTS TechLab. We thank Michael A. Klatt and Nicolas François for fruitful discussions and Stuart Ramsden for visualizing the hyperuniform system in Fig. 1.

Supplementary Material

Supplementary material is available at *PNAS Nexus* online.

Funding

S.H. and M.S. acknowledge that this research was partially supported by the Australian Research Council through the ARC Training Centre for Multiscale 3D Imaging, Modelling, and Manufacturing (M3D Innovation, Project IC # 180100008). C.N. and S.O. acknowledge that the research was supported by the Australian Research Council's Discovery Projects funding scheme (Project No. # DP200100358).

Author Contributions

S.H.: conceptualization, methodology, software, validation, formal analysis, investigation (detailed theoretical & numerical), data curation, visualization, writing—original draft, writing—review & editing. C.N.: conceptualization, methodology, software, validation, formal analysis, investigation (detailed numerical & experimental), data curation, visualization, writing—original draft, writing—review & editing. S.O.: conceptualization, methodology, investigation, validation, supervision, writing—review & editing, resources, project administration, funding acquisition. M.S.: conceptualization, methodology, investigation, validation, supervision, visualization, writing—original draft, writing—review & editing, resources, project administration, funding acquisition.

Data Availability

The data required to reproduce the results in this study are provided in the main text and Supplementary materials. The code for implementing Lloyd's algorithm, performing computational analyses, and STL geometry files compatible with CAD/FE software are available in the following GitHub repository: https://github.com/YeoniH/geometry-driven-hyperuniformity.

References

1 Gabrielli A, Joyce M, Labini FS. 2002. Glass-like universe: real-space correlation properties of standard cosmological models. *Phys Rev D*. 65(8):083523.

2 Torquato S, Stillinger FH. 2003. Local density fluctuations, hyperuniformity, and order metrics. *Phys Rev E*. 68(4):041113.

3 Huang M, Hu W, Yang S, Liu Q-X, Zhang HP. 2021. Circular swimming motility and disordered hyperuniform state in an algae system. *Proc Natl Acad Sci U S A*. 118(18):e2100493118.

4 Tjhung E, Berthier L. 2015. Hyperuniform density fluctuations and diverging dynamic correlations in periodically driven colloidal suspensions. *Phys Rev Lett*. 114(14):148301.

5 Chremos A, Douglas JF. 2017. Particle localization and hyperuniformity of polymer-grafted nanoparticle materials. *Ann Phys*. 529(5):1600342.

6 Wilken S, Guerra RE, Pine DJ, Chaikin PM. 2020. Hyperuniform structures formed by shearing colloidal suspensions. *Phys Rev Lett*. 125(14):148001.

7 Atkinson S, Zhang G, Hopkins AB, Torquato S. 2016. Critical slowing down and hyperuniformity on approach to jamming. *Phys Rev E*. 94(1):012902.

8 Klatt MA, *et al.* 2019. Universal hidden order in amorphous cellular geometries. *Nat Commun*. 10(1):811.

9 Hexner D, Levine D. 2015. Hyperuniformity of critical absorbing states. *Phys Rev Lett*. 114(11):110602.

10 Martelli F, Torquato S, Giovambattista N, Car R. 2017. Large-scale structure and hyperuniformity of amorphous ices. *Phys Rev Lett*. 119(13):136002.

11 Donev A, Stillinger FH, Torquato S. 2005. Unexpected density fluctuations in jammed disordered sphere packings. *Phys Rev Lett*. 95(9):090604.

12 Zachary CE, Jiao Y, Torquato S. 2011. Hyperuniform long-range correlations are a signature of disordered jammed hard-particle packings. *Phys Rev Lett*. 106(17):178001.

13 Jiao Y, *et al.* 2014. Avian photoreceptor patterns represent a disordered hyperuniform solution to a multiscale packing problem. *Phys Rev E*. 89(2):022721.

14 Zheng Y, *et al.* 2020. Disordered hyperuniformity in two-dimensional amorphous silica. *Sci Adv*. 6(16):eaba0826.

15 Toh C-T, *et al.* 2020. Synthesis and properties of free-standing monolayer amorphous carbon. *Nature*. 577(7789):199–203.

16 Florescu M, Torquato S, Steinhardt PJ. 2009. Designer disordered materials with large, complete photonic band gaps. *Proc Natl Acad Sci U S A*. 106(49):20658–20663.

17 Man W, *et al.* 2013. Isotropic band gaps and freeform waveguides observed in hyperuniform disordered photonic solids. *Proc Natl Acad Sci U S A*. 110(40):15886–15891.

18 Froufe-Pérez LS, *et al.* 2016. Role of short-range order and hyperuniformity in the formation of band gaps in disordered photonic materials. *Phys Rev Lett*. 117(5):053902.

19 Klatt MA, Steinhardt PJ, Torquato S. 2021. Gap sensitivity reveals universal behaviors in optimized photonic crystal and disordered networks. *Phys Rev Lett*. 127:037401.

20 Le Thien Q, McDermott D, Reichhardt CJO, Reichhardt C. 2017. Enhanced pinning for vortices in hyperuniform pinning arrays and emergent hyperuniform vortex configurations with quenched disorder. *Phys Rev B*. 96:094516.

21 Krishna S, Gopinath A, Bhattacharjee SM. 2022. Ordering and topological defects in social wasps' nests. *Sci Rep*. 12(1):12901.

22 Sharma V, Crne M, Park JO, Srinivasarao M. 2009. Structural origin of circularly polarized iridescence in jeweled beetles. *Science*. 325(5939):449–451.

23 Meyer JC, *et al.* 2008. Direct imaging of lattice atoms and topological defects in graphene membranes. *Nano Lett*. 8(11):3582–3586.

24 Torquato S. 2018. Hyperuniform states of matter. *Phys Rep*. 745:1–95.

25 Oğuz EC, Socolar JES, Steinhardt PJ, Torquato S. 2017. Hyperuniformity of quasicrystals. *Phys Rev B*. 95(5):054119.

26 Gray R. 1984. Vector quantization. *IEEE ASSP Mag*. 1(2):4–29.

27 Likas A, Vlassis N, Verbeek JJ. 2003. The global k-means clustering algorithm. *Pattern Recognit*. 36(2):451–461.

28 Lu L, Sun F, Pan H, Wang W. 2012. Global optimization of centroidal voronoi tessellation with Monte Carlo approach. *IEEE Trans Vis Comput Graph*. 18(11):1880–1890.

29 Oberst S, Evans TA, Lai JCS. 2014. Novel method for pairing samples in choice tests. *PLoS One*. 9(2):1–7.

30 Frenkel D. 1999. Entropy-driven phase transitions. *Physica A: Stat Mech Appl*. 263(1):26–38Proceedings of the 20th IUPAP International Conference on Statistical Physics.

31 van Anders G, Klotsa D, Ahmed NK, Engel M, Glotzer SC. 2014. Understanding shape entropy through local dense packing. *Proc Natl Acad Sci U S A*. 111(45):E4812–E4821.

32 Harper ES, van Anders G, Glotzer SC. 2019. The entropic bond in colloidal crystals. *Proc Natl Acad Sci U S A*. 116(34):16703–16710.

33 Klishin AA, van Anders G. 2020. When does entropy promote local organization? *Soft Matter*. 16(28):6523–6531.

34 Hong S, Klatt MA, Schröder-Turk G, François N, Saadatfar M. 2021. Dynamical arrest of topological defects in 2D hyperuniform disk packings. *EPJ Web Conf*. 249:15002.

35 Schroeder TBH, Houghtaling J, Wilts BD, Mayer M. 2018. It's not a bug, it's a feature: functional materials in insects. *Adv Mater*. 30(19):1705322.

36 Stuart-Fox D, *et al*. 2022. Bio-informed materials: three guiding principles for innovation informed by biology. *Nat Rev Mater*. 8(9):565–567.

37 Yan X, Zhuang L, Zhu Z, Yao X. 2021. Defect engineering and characterization of active sites for efficient electrocatalysis. *Nanoscale*. 13(6):3327–3345.

38 Mohammed MA, Grover P. 2022. Phase space analysis of nonlinear wave propagation in a bistable mechanical metamaterial with a defect. *Phys Rev E*. 106:054204.

39 Weaire DL, Hutzler S. 2001. *The physics of foams*. Clarendon Press.

40 Chieco AT, Durian DJ. 2021. Quantifying the long-range structure of foams and other cellular patterns with hyperuniformity disorder length spectroscopy. *Phys Rev E*. 103(6):062609.

41 Stoyan D, Kendall WS, Chiu SN, Mecke J. 2013. *Stochastic geometry and its applications*. Wiley series in probability and statistics. Wiley.

42 Kim D, Seol Y, Kim Y. 2021. Numerical study on rheology of two-dimensional dry foam. *Phys Fluids*. 33(5):052111.

43 Fletcher AG, Osterfield M, Baker RE, Shvartsman SY. 2014. Vertex models of epithelial morphogenesis. *Biophys J*. 106(11):2291–2304.

44 Bi D, Lopez JH, Schwarz JM, Manning ML. 2014. Energy barriers and cell migration in densely packed tissues. *Soft Matter*. 10: 1885–1890.

45 Bi D, Lopez JH, Schwarz JM, Manning ML. 2015. A density-independent rigidity transition in biological tissues. *Nat Phys*. 11(12):1074–1079.

46 Krajnc M, Stern T, Zankoc C. 2021. Active instability and nonlinear dynamics of cell-cell junctions. *Phys Rev Lett*. 127: 198103.

47 Zhou Y, Milner ST. 2015. T1 process and dynamics in glass-forming hard-sphere liquids. *Soft Matter*. 11:2700–2705.

48 Zhou Y, Milner ST. 2018. A geometrical criterion for glass transition in soft-sphere fluids. *Soft Matter*. 14:7075–7082.

49 Duclut C, Paijmans J, Inamdar MM, Modes CD, Jülicher F. 2022. Active t1 transitions in cellular networks. *Eur Phys J E*. 45(3):29.

50 Zhou Y, Milner ST. 2016. Structural entropy of glassy systems from graph isomorphism. *Soft Matter*. 12:7281–7288.

51 Culha U, Davidson ZS, Mastrangeli M, Sitti M. 2020. Statistical reprogramming of macroscopic self-assembly with dynamic boundaries. *Proc Natl Acad Sci U S A*. 117(21):11306–11313.

52 Anikeenko AV, Medvedev NN, Aste T. 2008. Structural and entropic insights into the nature of the random-close-packing limit. *Phys Rev E*. 77(3):031101.

53 McKay BD, Piperno A. 2014. Practical graph isomorphism, II. *J Symb Comput*. 60:94–112.

54 Li S, Zhao D, Niu H, Zhu X, Zang J. 2018. Observation of elastic topological states in soft materials. *Nat Commun*. 9(1):1370.

55 Denkov ND, Tcholakova SS, Höhler R, Cohen-Addad S. 2012. Foam rheology. In: Stevenson P, editor. *Foam engineering: fundamentals and applications*. Chichester: Wiley. p. 91–120.

56 Weaire D, Hutzler S, Drenckhan W, Saugey A, Cox SJ. 2006. The rheology of foams. In: Richtering W, editor. *Smart colloidal materials*. Berlin: Springer. p. 100–105.

57 Hutzler S, Saadatfar M, van der Net A, Weaire D, Cox SJ. 2008. The dynamics of a topological change in a system of soap films. *Colloids Surf A Physicochem Eng Asp*. 323(1-3):123–131.

58 Yan L. 2018. Entropy favors heterogeneous structures of networks near the rigidity threshold. *Nat Commun*. 9(1):1359.

59 Ellis RJ, Minton AP. 2003. Cell biology: join the crowd. *Nature*. 425(6953):27–28.

60 Weiss M, Elsner M, Kartberg F, Nilsson T. 2004. Anomalous subdiffusion is a measure for cytoplasmic crowding in living cells. *Biophys J*. 87(5):3518–3524.

61 Mardoum WM, Gorczyca SM, Regan KE, Wu T-C, Robertson-Anderson RM. 2018. Crowding induces entropically-driven changes to DNA dynamics that depend on crowder structure and ionic conditions. *Front Phys*. 6:53.

62 Onsager L. 1949. The effects of shape on the interaction of colloidal particles. *Ann N Y Acad Sci*. 51(4):627–659.

63 Frenkel D. 2015. Order through entropy. *Nat Mater*. 14(1):9–12.

64 Du CX, van Anders G, Newman RS, Glotzer SC. 2017. Shape-driven solid–solid transitions in colloids. *Proc Natl Acad Sci U S A*. 114(20):E3892–E3899.

65 Zhu G, *et al*. 2021. Self-similar mesocrystals form via interface-driven nucleation and assembly. *Nature*. 590(7846):416–422.

66 Saadatfar M, Takeuchi H, Robins V, Francois N, Hiraoka Y. 2017. Pore configuration landscape of granular crystallization. *Nat Commun*. 8(1):15082.

67 Francois N, Saadatfar M, Cruikshank R, Sheppard A. 2013. Geometrical frustration in amorphous and partially crystallized packings of spheres. *Phys Rev Lett*. 111(14):148001.

68 Hanifpour M, Francois N, Vaez Allaei SM, Senden T, Saadatfar M. 2014. Mechanical characterization of partially crystallized sphere packings. *Phys Rev Lett*. 113(14):148001.

69 Hanifpour M, *et al*. 2015. Structural and mechanical features of the order-disorder transition in experimental hard-sphere packings. *Phys Rev E*. 91(6):062202.

70 Schröder-Turk GE, *et al*. 2010. Disordered spherical bead packs are anisotropic. *Europhys Lett*. 90(3):34001.

71 Gkantzounis G, Amoah T, Florescu M. 2017. Hyperuniform disordered phononic structures. *Phys Rev B*. 95(9):094120.

72 Meeussen AS, Oğuz EC, Shokef Y, van Hecke M. 2020. Topological defects produce exotic mechanics in complex metamaterials. *Nat Phys*. 16(3):307–311.

73 Arango-Restrepo A, Rubi JM. 2020. Entropic transport in a crowded medium. *J Chem Phys*. 153(3):034108.

74 Romero-García V, *et al*. 2021. Wave transport in 1d stealthy hyperuniform phononic materials made of non-resonant and resonant scatterers. *APL Mater*. 9(10):101101.

75 Chen D, *et al*. 2021. Stone-Wales defects preserve hyperuniformity in amorphous two-dimensional networks. *Proc Natl Acad Sci U S A*. 118(3):e2016862118.

76 Kader MA, *et al*. 2020. Novel design of closed-cell foam structures for property enhancement. *Addit Manuf*. 31:100976.

77 Francois N, *et al*. 2014. Experimental investigation of the mechanical stiffness of periodic framework-patterned elastomers. *Philos Trans R Soc A Math Phys Eng Sci*. 372(2008):20120035.

78 Fan H, Xia B, Tong L, Zheng S, Yu D. 2019. Elastic higher-order topological insulator with topologically protected corner states. *Phys Rev Lett*. 122(20):204301.

79 Xu W, Qin L, Zhang W, Wang J. 2023. Acoustic Fano-like resonance phenomenon based local resonance generated by soft material cylinder. *Appl Phys A*. 129(3):213.

80 Yang L, *et al.* 2022. Robust Fano resonance between mechanical first- and second-order topological states. *Int J Mech Sci*. 236: 107768.

81 Kronowetter F, *et al.* 2023. Realistic prediction and engineering of high-Q modes to implement stable Fano resonances in acoustic devices. *Nat Commun*. 14(1):6847.

82 Zaki SE, Mehaney A, Hassanein HM, Aly AH. 2020. Fano resonance based defected 1D phononic crystal for highly sensitive gas sensing applications. *Sci Rep*. 10(1):17979.

83 Kvashnin AG, Sorokin PB, Kvashnin DG. 2010. The theoretical study of mechanical properties of graphene membranes. *Fuller Nanotub Car Nanostructures*. 18(4-6):497–500.

84 Savin AV, Kivshar YS. 2013. Localized defect modes in graphene. *Phys Rev B*. 88(12):125417.

85 Zandiatashbar A, *et al.* 2014. Effect of defects on the intrinsic strength and stiffness of graphene. *Nat Commun*. 5(1):3186.

86 Torquato S. 2010. Reformulation of the covering and quantizer problems as ground states of interacting particles. *Phys Rev E*. 82(5):056109.

87 Schröder-Turk GE, *et al.* 2011. Minkowski tensor shape analysis of cellular, granular and porous structures. *Adv Mater*. 23(22–23): 2535–2553.

88 Nerse C, Oberst S, Moore S, MacGillivray I. 2022. Assessment of flanking transmissions in measurements of sound transmission loss of multilayer panels.

89 Zhu Q. 2021. A case study on the transmission loss suite in the University of Technology Sydney. p. 23–30.

90 Steinier J, Termonia Y, Deltour J. 1972. Smoothing and differentiation of data by simplified least square procedure. *Anal Chem*. 44(11):1906–1909.